Catalytic Carbon Monoxide Oxidation over Potassium-Doped Manganese Dioxide Nanoparticles Synthesized by Spray Drying

Kevin Ollegott [1] · Niklas Peters [1] · Hendrik Antoni [1] · Martin Muhler [1]

Abstract

Manganese oxides are promising catalysts for the oxidation of CO as well as the removal of volatile organic compounds from exhaust gases because of their structural versatility and their ability to reversibly change between various oxidation states. MnO_2 nanoparticles doped with Na^+ or K^+ were synthesized by a semi-continuous precipitation method based on spray drying. Specific surface area, crystallite size, and morphology of these particles were predominantly determined by the spray-drying parameters controlling the quenching of the crystallite growth, whereas thermal stability, reducibility, and phase composition were strongly influenced by the alkali ion doping. Pure α-MnO_2 was obtained by K^+ doping under alkaline reaction conditions followed by calcination at 450 °C, which revealed a superior catalytic activity in comparison to X-ray amorphous or Mn_2O_3-containing samples. Thus, the phase composition is identified as a key factor for the catalytic activity of manganese oxides, and it was possible to achieve a similar activation of a K^+-doped X-ray amorphous catalyst under reaction conditions resulting in the formation of crystalline α-MnO_2. The beneficial effect of K^+ doping on the catalytic activity of MnO_2 is mainly associated with the stabilizing effect of K^+ on the α-MnO_2 tunnel structure.

1 Introduction

Catalysts containing noble metals like palladium, platinum, or rhodium are frequently applied for industrial oxidation reactions [1, 2]. CO oxidation is of special interest, as it is applied for exhaust gas purification, indoor air cleaning, or preferential CO removal from H_2-containing feed gases [3]. CO oxidation is also a key reaction for the purification of automotive exhaust gases in the three-way catalytic converter [4–6]. Furthermore, it is a common model reaction to understand catalytic mechanisms and to evaluate catalytic performance [7]. However, noble metal-based catalysts often suffer from poisoning, high sintering rates, low thermal stability, and high

cost. Therefore, non-precious metal oxides have attracted considerable interest as a low-cost alternative for these oxidation reactions. Manganese oxides are a highly promising class of materials as they are known to be catalytically active in several oxidation reactions such as the oxidation of CO [8, 9], soot [10], or hydrocarbons [11]. Due to its numerous stable oxidation states (II, III, IV), Mn can form a variety of different oxides with the most common ones being MnO, Mn_3O_4, Mn_2O_3, and MnO_2 [7, 12]. Especially MnO_2 forms several polymorphic structures such as α-, β-, γ-, δ-, ε-, and λ-MnO_2, which can have a strong influence on the catalytic activity [9, 13, 14]. All MnO_2 polymorphic forms are built from MnO_6 octahedral units, which are linked in different ways [13]. Depending on the connection by sharing edges or corners, different structural arrangements can be formed, most of which can be described as tunnel or layer structures [15]. α-MnO_2 features double chains of edge-sharing MnO_6 octahedra forming 2×2 open tunnel structures with dimensions of 4.6 Å × 4.6 Å [15]. These tunnels can incorporate cations such as K^+ and Na^+ or other small molecules, which are surrounded by eight oxygen atoms and have a stabilizing effect on the tunnel structure of α-MnO_2 [16, 17]. On the other hand, β-
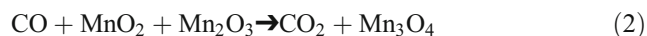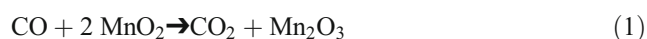
✉ Martin Muhler
muhler@techem.rub.de

[1] Laboratory of Industrial Chemistry, Ruhr-University Bochum, Universitätsstr. 150, 44780 Bochum, Germany

MnO_2 cannot incorporate cations as it consists of single strands of edge-sharing octahedral units, which form 1×1 tunnels with a size of 1.89 Å. γ-MnO_2 forms 2×1 tunnels and δ-MnO_2 is characterized by a two-dimensional layer structure with an interlayer distance of up to 7 Å [15].

The reaction mechanism of CO oxidation over MnO_2 catalysts is still under debate. Usually, a Mars-van Krevelen-type mechanism involving lattice oxygen is assumed [8, 9, 18, 19]. The corresponding reaction pathway proposed by Liang et al. [9] is described in Eqs. 1–4. The CO molecule is supposed to adsorb with its C atom coordinated to a surface O atom of MnO_2. By breaking the corresponding Mn–O bond, CO_2 is formed and MnO_2 is reduced to Mn_2O_3 (Eq. 1). These steps can be repeated at the same Mn site yielding Mn_3O_4 (Eq. 2) The generated O vacancies are re-oxidized by either gas-phase O adsorbing on the surface site directly or by diffusion of lattice oxygen anions within the material to regain MnO_2 (Eqs. 3–4) [9].

$$CO + 2\,MnO_2 \rightarrow CO_2 + Mn_2O_3 \tag{1}$$

$$CO + MnO_2 + Mn_2O_3 \rightarrow CO_2 + Mn_3O_4 \tag{2}$$

$$2\,Mn_3O_4 + O_2 \rightarrow 2\,MnO_2 + Mn_2O_3 \tag{3}$$

$$2\,Mn_2O_3 + O_2 \rightarrow 4\,MnO_2 \tag{4}$$

Ramesh et al. [8] propose that either a Langmuir-Hinshelwood or a Eley-Rideal mechanism is the dominant reaction pathway of CO oxidation over MnO_2 and Mn_2O_3 catalysts. A Mars-van Krevelen-type mechanism may occur simultaneously but is only predominant over MnO catalysts.

The high catalytic activity reported for Mn oxides is often associated with their structural versatility and the ability of Mn to reversibly change between various oxidation states. Furthermore, high oxygen mobility in the lattice as well as a high oxygen storage capability is reported for Mn oxides [8, 20, 21]. The catalytic performance of MnO_2 catalyts can be significantly influenced by the Mn–O bond strength. Liang et al. [9] investigated the influence of the MnO_2 polymorphism on the catalytic performance in CO oxidation. It was shown that the catalytic activity improved in the order of β- < γ- < δ- $\approx$ α-MnO_2 correlated with the Mn–O bond strength of the polymorphs.

In this work, we report on the synthesis of MnO_2 catalysts by semi-continuous precipitation method in a micromixer coupled with a spray dryer. The method is based on the comproportionation of either $KMnO_4$ or $NaMnO_4$ with Mn(NO3)2. The precursor solutions are rapidly mixed in a T-shaped micromixer assuring a defined mixing time, followed by rapid quenching of the reaction by spray drying. The structural properties of the catalysts were characterized by atomic absorption spectroscopy (AAS), X-ray diffraction (XRD), N_2 physisorption, scanning electron microscopy (SEM), X-ray photoelectron spectroscopy (XPS), and temperature-programmed reduction (TPR) with H_2 and CO. CO oxidation is used as a probe reaction to evaluate the catalytic performance and to derive structure-activity correlations. Especially, the influence of the incorporated alkali ions Na^+ and K^+ on the structure and consequently the catalytic performance was studied in detail.

2 Experimental

2.1 Catalyst Synthesis by Spray Drying

MnO_2 catalysts were prepared by a semi-continuous precipitation method based on the comproportionation of $KMnO_4$ (Sigma Aldrich, purity $\geq 99.0\%$) and $Mn(NO_3)_2$ (Sigma-Aldrich, purity $\geq 97.0\%$). A 0.011 M solution of $KMnO_4$ in either water (N) or in 0.01 M KOH solution (OH) and a 0.016 M solution of $Mn(NO_3)_2$ in water were rapidly mixed in a micromixer. For each solution, a continuous flow of 3 mL min^{-1} was used. The emerging brown suspension was quenched by spray drying (Mini spray dryer B-290, Büchi) to inhibit further particle growth. A schematic illustration of the spray dryer and the micromixer is shown in Fig. 1. Intermittent washing of the micromixer with a saturated oxalic acid solution was performed every 20 min to avoid plugging. The received particles were washed with water (ultra-high purity) and dried at 373 K for 12 h. The samples were used as prepared (K-N-MnO_2, K-OH-MnO_2) or calcined at 450 °C or 500 °C for 4 h in synthetic air (K-N/OH-MnO_2-450, K-N/OH-MnO_2-500). The synthesis was performed analogously using $NaMnO_4$ and NaOH (Na-N/OH-MnO_2).

2.2 Structural Characterization

The XRD patterns were recorded using an Empyrean theta-theta powder diffractometer (PANalytical) with Cu K$_\alpha$ radiation ($\lambda = 1.5406$ Å, 45 kV, 40 mA). The powders were investigated in the range of 10° to 80° 2θ with a step width of 0.026° 2θ. The obtained XRD patterns were analyzed with the PANalytical X'pert HighScore Plus v.3.0 software.

Nitrogen physisorption measurements were performed in a BELSORP-mini measurement system (BEL Japan Inc.) at a constant temperature of 77 K. The samples used in a grain fraction of 250–355 μm were pretreated at 250 °C for 2 h at reduced pressure to remove adsorbed water. The specific surface areas were derived from the adsorption isotherm using the BET method. The total pore volume was obtained by applying the BJH method.

AAS was carried out with a SpectrAA 220 (Variant) spectrometer to determine the amount of residual Na and K using the corresponding hollow cathode lamps.

TPR experiments with H_2 were performed in a flow setup equipped with a thermal conductivity detector (Hydros,
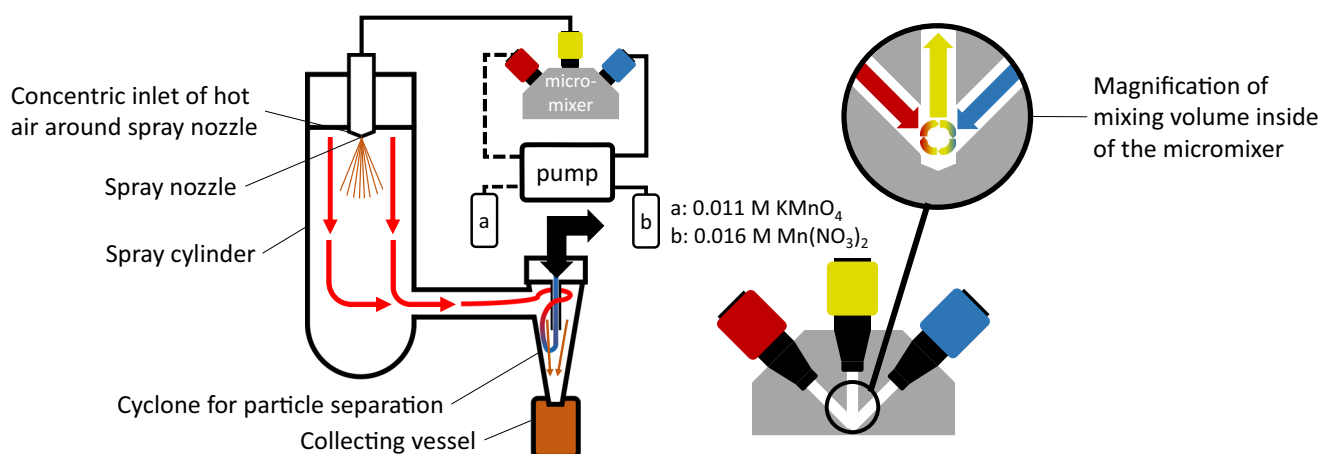
Fig. 1 Schematic illustration of the spray dryer (left) and the micromixer (right)

Fisher-Rosemount) analyzing the H_2 concentration in the effluent gas. One hundred milligrams of the samples (250–355 μm) were heated to 600 °C in a flow of 4.59% H_2 balanced in Ar with a heating rate of 5 K min^{-1}. A total volumetric flow rate of 84.1 mL min^{-1} was used. For the TPR experiments with CO 20 mg of the catalyst (250–355 μm) diluted with 80mg silicon carbide were heated to 450 °C in a flow of 4.83% CO balanced in He with a heating rate of 5 K min^{-1}. A total volumetric flow rate of 50 mL min^{-1} was used.

XPS measurements were carried out in an ultra-high vacuum setup equipped with a high-resolution Gammadata-Scienta SES 2002 analyzer. A monochromatic Al K_α X-ray source (1486.3 eV; anode operating at 14.5 eV and 30.5 mV) was used as incident radiation and pass energy of 200 eV was chosen resulting in an energy resolution better than 0.5 eV. Charging effects were compensated using a flood gun. Binding energies were calibrated by positioning the main C 1s peak at 284.5 eV.

Scanning electron microscopy images of the samples were acquired with a FEI eSEM Dual Beam Quanta 3D FEG operated at an acceleration voltage of 20 kV. The samples were loaded onto the sample holder using a carbon film.

2.3 Catalytic CO Oxidation

Catalytic CO oxidation experiments were performed in an all stainless-steel microreactor setup at ambient pressure. Pure He (purity > 99.999%), 9.98% CO (purity > 99.997%) in He and 20.01% O_2 (purity > 99.998%) in He were connected to the microreactor setup. All gas flows were adjusted by calibrated mass flow controllers (MFCs) and a mixing cross was used to produce diluted mixtures of CO and O_2 in He. The reactor unit featured a U-shaped quartz reactor with an inner diameter of 4 mm, which was heated in an aluminum block oven. A thermocouple placed directly next to the fixed bed was used for temperature control. A calibrated two channel non-dispersive

IR detector (Hartmann & Braun, URAS 14) measured the concentrations of CO and CO_2 in the effluent gas stream.

CO oxidation was performed in a mixture of 2% CO and 2% O_2 balanced in He with a total flow rate of 50 mL min^{-1}. The fixed bed contained 20 mg of the catalyst (250–355 μm) diluted with 80mg silicon carbide corresponding to a gas hourly space velocity of 150,000 mL g$^{-1}_{cat}$ h^{-1}. After purging the reactor with He, the reaction gas mixture was passed through the catalyst bed at ambient temperature for 30 min. Then, the catalyst was heated to either 300 °C or 450 °C with a heating rate of 1 K min^{-1}. The maximum temperature was held for 1 h. The sample was cooled to ambient temperature in the reaction gas mixture with a cooling rate of 1 K min^{-1}. Long-term CO oxidation experiments were performed analogously with a maximum temperature of 150 °C and a holding period of 125 h.

An oxidative pretreatment was performed for some samples prior to CO oxidation. The samples were heated to 450 °C in 20% O_2 balanced in He (20 mL min^{-1}) with a heating rate of 5 K min^{-1}. The temperature was kept constant for 1 h. Afterwards, the reactor was purged with He and cooled to ambient temperature.

3 Results

3.1 Elemental Analysis by Atomic Absorption Spectroscopy

The residual alkali metal contents of the uncalcined samples were determined by AAS and are summarized in Table 1. Despite the performed washing procedure, all four samples contain alkali metal residues. Both samples precipitated under alkaline conditions exhibit a considerably higher mass fraction of the respective alkali ions than K-N-MnO$_2$ or Na-N-MnO$_2$. This can be rationalized by the higher concentration of Na$^+$ and K$^+$ cations in the reaction solution during the alkaline

Table 1 Elemental analysis by atomic absorption spectroscopy

Sample	K content/wt%	Na content/wt%
K-N-MnO$_2$	2.7	–
K-OH-MnO$_2$	4.6	–
Na-N-MnO$_2$	–	1.2
Na-OH-MnO$_2$	–	3.6

precipitation. To further investigate the influence of the K$^+$ concentration and the pH value during the precipitation, one batch of K-N-MnO$_2$ was synthesized in a 0.01 M KNO$_3$ solution. This sample contains 2.6 wt% K, indicating that the alkaline conditions are needed to facilitate the intercalation of K$^+$ into the structure of MnO$_2$. Under alkaline conditions, the surface charge of MnO$_2$ is altered, which may cause this facilitating effect.

The presence of residual nitrate ions can be excluded by TPO experiments (not shown) as the formation of NO or NO$_2$ cannot be detected, suggesting that Na$^+$ and K$^+$ are incorporated into the MnO$_2$ structure and are not present in the form of nitrate salts.

3.2 X-Ray Diffraction

The XRD patterns of the synthesized samples are shown in Fig. 2 for the K-containing catalysts and in Fig. 3 for the Na-containing catalysts. Reference patterns for α-MnO$_2$ (PDF 00-044-0141) and α-Mn$_2$O$_3$ (PDF 01-073-1826) are included in all graphs. The obtained XRD patterns of the four uncalcined samples are almost identical and indicate a low degree of crystallinity. Broad reflections with low intensities are observed for all samples. One main reflection at 37.2° can be identified and assigned to the main (211) reflection of the α-MnO$_2$ (37.5°). As the observed reflection is shifted to lower 2θ values, it is assumed that the interplanar distance in the synthesized samples is larger compared with the reference. Three additional reflections are observed at 42.5°, 56.6°, and 66.7°, which can also be assigned to α-MnO$_2$. However, these reflections do not have the expected relative intensities, and other strong reflections from the α-MnO$_2$ reference cannot be observed. This may be caused by an anisotropic crystallite growth during the rapid precipitation and spray drying. Therefore, distinct phase identification is not possible for the uncalcined samples.

After calcination, the XRD patterns show sharper reflections with higher intensities due to an increased degree of crystallinity compared with the uncalcined samples. For both K-OH-MnO$_2$-450 and K-OH-MnO$_2$-500, the reflections can be assigned to pure α-MnO$_2$ as no additional reflections can be observed. Based on the recorded XRD pattern, α-MnO$_2$ is also the main phase of Na-OH-MnO$_2$-450 and Na-OH-MnO$_2$-500. An additional small reflection at 33.1° indicates the presence of a small amount of the α-Mn$_2$O$_3$ phase for Na-OH-MnO$_2$-500. The α-MnO$_2$ phase formed by the calcination of Na-OH-MnO$_2$ is thermally less stable than the α-MnO$_2$ phase formed from K-OH-MnO$_2$ and transforms to α-Mn$_2$O$_3$ during calcination at 500 °C. For K-N-MnO$_2$-450 characteristic, reflections of α-MnO$_2$ are observed at 12.9°, 18.2°, 28.8°, and 37.6°. However, compared with the XRD patterns of K-OH-MnO$_2$-450/500, the reflections at 25.8°, 36.6°, and 39.1° are less pronounced indicating a lower degree of crystallinity. The
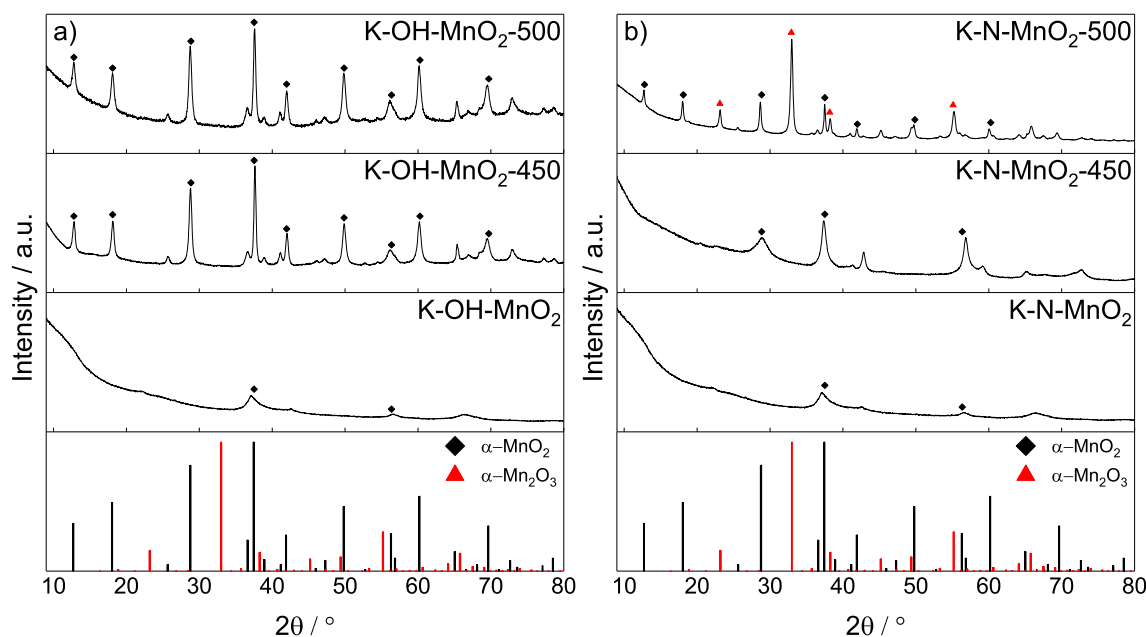

Fig. 2 XRD patterns of K-OH-MnO$_2$ (**a**) and K-N-MnO$_2$ (**b**) as received and after calcination at 450 °C and 500 °C. References are displayed as vertical lines in black for α-MnO$_2$ (PDF 00-044-0141) and in red for α-Mn$_2$O$_3$ (PDF 01-073-1826)
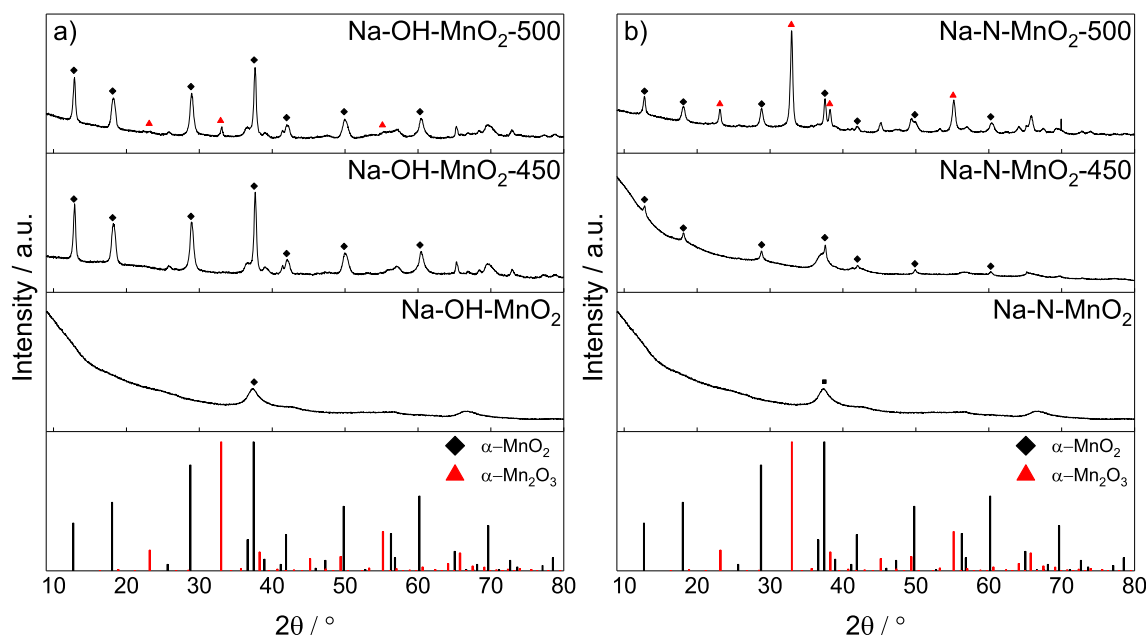
Fig. 3 XRD patterns of Na-OH-MnO$_2$ (**a**) and Na-N-MnO$_2$ (**b**) as received and after calcination at 450 °C and 500 °C. References are displayed as vertical lines in black for α-MnO$_2$ (PDF 00-044-0141) and in red for α-Mn$_2$O$_3$ (PDF 01-073-1826)

XRD pattern of K-N-MnO$_2$-500 shows reflections at 12.9°, 18.2°, 28.8°, and 37.6° assigned to α-MnO$_2$ and reflections at 23.2°, 33.1°, and 55.2° assigned to α-Mn$_2$O$_3$, indicating that a mixture of both phases is present in the sample. As the strongest reflection of K-N-MnO$_2$-500 at 33.1° is due to α-Mn$_2$O$_3$, it is suggested that this is the main phase of the mixture. For Na-N-MnO$_2$, reflections at 12.9°, 18.2°, 28.8°, and 37.6° can be observed indicating the presence of α-MnO$_2$. The reflection at 37.6° superimposes with the broad reflections at 37.2° of the uncalcined samples. The phase transformation from the as-received X-ray amorphous phase to α-MnO$_2$ is incomplete, and a phase without a distinct crystal structure is still present. The obtained XRD pattern of Na-N-MnO$_2$-500 is similar to the one of K-N-MnO$_2$-500 indicating that α-Mn$_2$O$_3$ is the main phase in a mixture of α-MnO$_2$ and α-Mn$_2$O$_3$.

The average crystallite size of the samples was derived based on the XRD patterns using the Scherrer equation. To determine the crystallite size of the α-MnO$_2$ phases, the reflection at 37.5° is used. For sample-containing α-Mn$_2$O$_3$, the reflection at 32.9° is used in addition. The results are summarized in Table 2. A crystallite size between 3.6 nm and 5.6 nm is estimated for the uncalcined samples. Thus, the quenching of the precipitation reaction caused by spray drying prevents the growth of larger crystallites. It has to be noted that the obtained crystallite sizes of the uncalcined samples can only be taken as a rough estimate. After calcination at 450 °C, the crystallite size is increased for all samples indicating crystallite growth. Further calcination at 500 °C does not significantly change the crystallite size. A slight increase is observed for K-N-MnO$_2$ and Na-N-MnO$_2$. The crystallite sizes of K-OH-MnO$_2$-450 and K-OH-MnO$_2$-500 are almost identical, further

emphasizing the thermal stability of the obtained α-MnO$_2$ structure. The crystallite sizes of the formed α-Mn$_2$O$_3$ phase of K-N-MnO$_2$-500, Na-N-MnO$_2$-500, and Na-OH-MnO$_2$-500 are comparable to the size of the α-MnO$_2$ crystallites.

3.3 N$_2$ Physisorption Results

The results of the N$_2$ physisorption measurements are summarized in Table 3. The specific surface areas range from 28 to 93 m^2 g^{-1}. K-N-MnO$_2$ and K-OH-MnO$_2$ have a specific surface area of approximately 80 m^2 g^{-1}, whereas Na-N-MnO$_2$ and Na-OH-MnO$_2$ have a slightly larger specific surface area of roughly 90 m^2 g^{-1}. The exchange of K to Na during the precipitation seems to increase the specific surface area of the samples. However, the samples precipitated under neutral and under alkaline conditions have similar specific surface areas, an influence of the amount of the alkali metal on the specific surface area can be excluded. Due to calcination, K-OH-MnO$_2$-450 and K-OH-MnO$_2$-500 have significantly smaller specific surface areas of 37 m^2 g^{-1} and 28 m^2 g^{-1}, respectively. Similar trends can be observed for the derived pore volumes. K-N-MnO$_2$ and K-OH-MnO$_2$ have an identical pore volume of 0.17 m^2 g^{-1}, which decreases during calcination to 0.12 m^2 g^{-1} at 450 °C and 0.08 m^2 g^{-1} at 500 °C. In contrast, Na-OH-MnO$_2$ has a significantly larger pore volume than Na-N-MnO$_2$.

The N$_2$ adsorption and desorption isotherms are shown in the supporting information. For all uncalcined samples, pseudo-type II isotherms with H3 hysteresis loops are observed [22], indicating loose agglomerates of plate-like particles, which form slit-like pores with a low degree of pore

Table 2 Average crystallite sizes derived from the XRD patterns

Sample	Crystallite size/nm			
	Uncalcined	450 °C	500 °C	
	α-MnO$_2$ (37.2°)	α-MnO$_2$ (37.5°)	α-MnO$_2$ (37.5°)	α-Mn$_2$O$_3$ (32.9°)
K-N-MnO$_2$	5.2	23.4	34.6	23.8
K-OH-MnO$_2$	3.6	26.5	26.9	–
Na-N-MnO$_2$	4.7	20.4	24.8	23.2
Na-OH-MnO$_2$	5.6	22.6	21.9	28.4

curvature [22]. This observation provides further evidence for an anisotropic particle growth as concluded from the XRD results. Both calcined K-OH-MnO$_2$-450 and K-OH-MnO$_2$-500 samples show similar adsorption and desorption isotherms, but the hysteresis loop is less pronounced.

The pore size distributions derived from the BJH method are provided in the supporting information for all samples. All uncalcined samples show a sharp and very intense peak at 3.5 nm, which is caused by the tensile strength effect. Below a certain pressure, a macroscopic meniscus cannot exist anymore, and the remaining liquid evaporates spontaneously [23]. Therefore, a precise determination of the average pore diameter is not possible for the uncalcined samples. K-N-MnO$_2$, K-OH-MnO$_2$, and Na-N-MnO$_2$ exhibit an additional maximum at 2 nm. Beyond 5 nm, the distribution decreases as a function of the pore diameter indicating that most of the pores are in the range between 1 and 10 nm. Na-OH-MnO$_2$ shows a broader pore size distribution with more pores between 5 and 40 nm. The number of pores decreases above a pore diameter of approximately 25 nm. This broader pore size distribution explains the larger pore volume. The tensile strength effect cannot be observed for K-OH-MnO$_2$-450 and K-OH-MnO$_2$-500, which have a broad, almost flat pore size distribution between 2 and 40 nm, reaching its maximum at around 22 nm.

3.4 Scanning Electron Microscopy

SEM was applied to investigate the structure and morphology of selected samples. Fig. 4 shows the SEM images of K-OH-MnO$_2$, K-OH-MnO$_2$-450, and Na-OH-MnO$_2$. All three samples are characterized by rather spherical agglomerates with a size between 1 and 4 μm. The individual particles forming these agglomerates have a size between 100 and 300 nm. These dimensions are considerably larger than the crystallite sizes derived from the XRD patterns suggesting that the particles observed by SEM consist of multiple smaller crystallites which formed connected particles

during the spray drying. K-OH-MnO$_2$ has the smoothest surface of all three samples and shows less distinct individual particles compared with Na-OH-MnO$_2$ and K-OH-MnO$_2$-450. The surface morphology of K-OH-MnO$_2$-450 is rougher and exhibits several cavities with sizes between 200 and 500 nm. However, the observed particle dimensions and the morphology of K-OH-MnO$_2$ are not strongly changed by calcination. As all three samples are relatively similar, it can be concluded that their structure is primarily influenced by the initial precipitation and the quenching caused by the spray drying and not by the different alkali ions.

3.5 X-Ray Photoelectron Spectroscopy

XPS was used to investigate the oxidation states of K-OH-MnO$_2$ before and after calcination at 450 °C. A precise identification of manganese oxides by XPS is challenging due to the large number of different oxidation states, which only show small differences in their peak positions and shapes. Therefore, both the Mn 2p and the Mn 3s regions were investigated. The shape of the Mn 3p$_{3/2}$ peak as well as the multiplet separation of the Mn 3s peak provide information about the oxidation states [24–26]. The Mn 2p signal is split into the Mn 2p$_{3/2}$ and Mn 2p$_{1/2}$ peaks. Their position differs by less than 2 eV for the different oxidation states [24, 25]. Due to these variations spectra of Mn(II), Mn(II,III), Mn(III), and Mn(IV) reference materials were measured, which are shown in the supporting information. The obtained multiplet separations of the Mn 3s peak for the different oxidation states are summarized in Table 4.

The spectra of the Mn 2p and Mn 3s regions for K-OH-MnO$_2$ and K-OH-MnO$_2$-450 are presented in Fig. 5. The shape of the Mn 3p$_{3/2}$ peak of K-OH-MnO$_2$ at 642 eV with its distinct shoulder at 643 eV is similar to the peak shape of the Mn(IV) reference material. Furthermore, K-OH-MnO$_2$ exhibits a Mn 3s multiplet splitting of 4.9 eV, indicating Mn(IV). The peaks of K-OH-MnO$_2$-450 are shifted to lower binding energies indicating a slight change in the oxidation state. However, the peak shape of the Mn 2p$_{3/2}$ peak and the multiplet separation of the Mn 3s signal remain nearly unchanged.

Table 3 Structural properties derived by N_2 physisorption

Sample	Specific surface area/m² g⁻¹	Pore volume/cm³ g⁻¹
K-N-MnO₂	80	0.17
K-OH-MnO₂	77	0.17
K-OH-MnO₂-450	37	0.12
K-OH-MnO₂-500	28	0.08
Na-N-MnO₂	93	0.19
Na-OH-MnO₂	90	0.26

These results indicate that Mn(IV) is present in the surface-near region.

3.6 Temperature-Programmed Reduction with H_2 and CO

The H_2 TPR profiles are shown in Fig. 6 and reveal that the reduction of all samples starts at approximately 150 °C. Na-N-MnO₂ and Na-OH-MnO₂ show two distinct reduction peaks at about 270 °C and 370 °C, which can be attributed to the consecutive reduction of MnO_2 to Mn_3O_4 and of Mn_3O_4 to MnO, respectively [20]. The H_2 TPR profile of K-N-MnO₂ is similar to those of Na-N-MnO₂ and Na-OH-MnO₂, but the second reduction peak is shifted to a lower temperature of 308 °C superimposing with the first reduction peak at 280 °C. K-OH-MnO₂ shows its first peak of H_2 consumption at 273 °C, but the second reduction peak is further shifted to 293 °C overlapping strongly with the first peak. This shift of the second reduction peak may be caused by the higher K content of K-OH-MnO₂. Wu et al. [27] report a similar shift of reduction peaks for an increasing K content of manganese ores, suggesting that the alkali ions weaken the Mn–O bond and facilitate the reduction at lower temperatures. K-OH-MnO₂-450 containing pure α-MnO₂ shows a slightly different TPR profile with at least two reduction peaks superimposing. In contrast to the other samples, the first reduction peak at 296 °C has a lower intensity than the second peak at 316 °C. Therefore, α-MnO₂ may follow a different reduction pathway to MnO with Mn_3O_4 and Mn_2O_3 as intermediates [9]. MnO

was the final product of all reductions as indicated by the green color of the remaining solid.

The CO TPR profiles of Na-N-MnO₂, Na-OH-MnO₂, K-OH-MnO₂, and K-OH-MnO₂-450 are shown in Fig. 7. The overall reduction behavior of the samples is similar with either H_2 or CO and MnO still represents the final product [8]. The initial reduction peak of all samples during CO TPR is shifted to lower temperatures indicating that CO has a stronger reducing effect than H_2. Na-N-MnO₂, Na-OH-MnO₂, and K-OH-MnO₂ also show two distinct reduction peaks, which can be assigned to the two-step reduction of MnO_2 to MnO with Mn_3O_4 as an intermediate. The first reduction peak of all three samples has its maximum in the range of 160 to 195 °C. The CO TPR profiles of Na-N-MnO₂ and Na-OH-MnO₂ show the second reduction peak at 345 °C and 360 °C, respectively, which is only a slight shift to lower temperatures. K-OH-MnO₂ exhibits the second reduction peak also at 360 °C showing no shift in comparison to the CO TPR profiles of the Na-containing samples. During the TPR with CO, the promoting effect of an increasing K content cannot be verified indicating that H_2 and CO show different reduction behavior. K-OH-MnO₂-450 has a vastly different CO TPR profile with three reduction peaks at 275 °C, 320 °C, and 390 °C. This observation further supports the assumption that α-MnO₂ follows a three-step reduction pathway to MnO with Mn_2O_3 and Mn_3O_4 as intermediates. In comparison to the TPR with H_2, the second and third reduction peaks are shifted to higher temperatures.

The specific H_2 and CO consumption and the degrees of reduction for these samples are summarized in Table 5. The degree of reduction is defined as the ratio of the actual H_2 or CO consumption obtained from the TPR profiles to the theoretical H_2 or CO consumption of pure MnO_2 to MnO (Eqs. 5–6):

$$MnO_2 + H_2 \rightarrow MnO + H_2O \tag{5}$$

$$MnO_2 + CO \rightarrow MnO + CO_2 \tag{6}$$

Despite the shift in reduction temperature, all four uncalcined samples exhibit a similar degree of reduction of
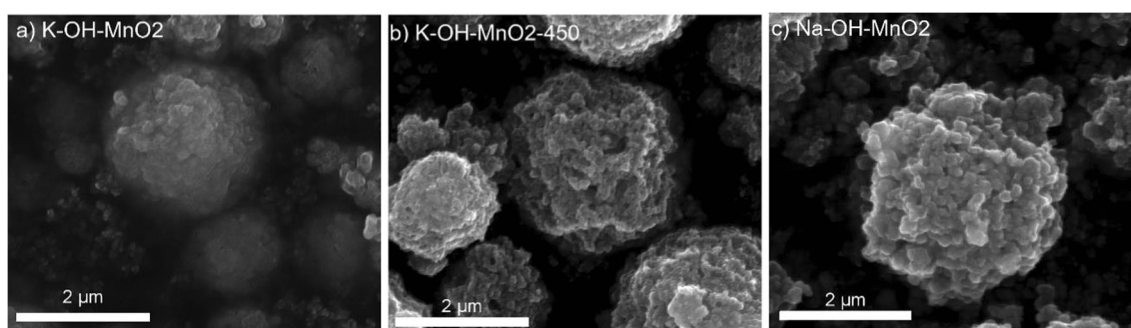

Fig. 4 SEM images of K-OH-MnO₂, K-OH-MnO₂-450, and Na-OH-MnO₂

Table 4 Mn 3s multiplet splitting for Mn(II), Mn(II,III), Mn(III), and Mn(IV) reference materials

Material	Mn 3s multiplet separation ΔE/eV
Mn(II)/MnO	5.9
Mn(II,III)/Mn_3O_4	5.9
Mn(III)/Mn_2O_3	5.5
Mn(IV)/MnO_2	4.8

approximately 70%, indicating oxygen deficiencies and defects in the MnO_2 crystal structure and being in good agreement with the low degree of crystallinity. K-OH-MnO_2-450 displays a higher degree of reduction of 82.2% indicating that additional oxygen was incorporated into the sample during calcination. The reduction degrees derived from the CO TPR profiles are comparable to the ones derived from the H_2 TPR profiles. The uncalcined samples exhibit a degree of reduction between 69% and 75%, whereas K-OH-MnO_2-450 has higher reduction degree of 85.2%.

3.7 CO Oxidation

For each sample, three-successive CO oxidation experiments with an initial feed gas of 2% CO and 2% O_2 were performed. During the first and the third experiment, the maximum temperature was 300 °C, whereas a maximum temperature of 450 °C was reached during the second CO oxidation. A commercial manganese copper-mixed oxide catalyst (Moleculite ®, Molecular Products Limited), which is designed for the oxidative removal of CO or volatile organic compounds (VOCs) serves as benchmark. Figure 8 shows the degree of CO conversion as a function of temperature during the first and third CO oxidation experiment. The CO conversion of the commercial catalyst is included as a dashed line in each graph. For a better comparison of the different samples, the obtained T_{50} and T_{100} values of the first and the third CO oxidation are summarized in Tables 6 and 7.

All uncalcined samples exhibit similar catalytic performance in the first CO oxidation experiment with T_{50} values between 213 °C and 227 °C during the heating ramp. K-N-MnO_2 achieves full conversion at 295 °C, whereas the other samples reach a maximum conversion of 93% at 300 °C. The K-containing samples K-N-MnO_2 and K-OH-MnO_2 have a slightly better performance as demonstrated by the lower T_{50} temperatures. The cooling curves of the first CO oxidation experiment of Na-N-MnO_2 and Na-OH-MnO_2 are shifted to higher temperatures, indicating a decrease in the catalytic performance. In contrast, the T_{50} temperatures of the K-containing samples are shifted to lower temperatures. K-OH-MnO_2-450 exhibits significantly better catalytic performance than the uncalcined samples with a T_{50} temperature of 132 °C. It reaches full conversion below 200 °C and is the only sample that shows a considerable conversion of 5% at 50 °C. Therefore, K-OH-MnO_2-450 is the only sample that has a lower T_{50} and T_{100} temperature than the commercial reference catalyst. Furthermore, K-OH-MnO_2-450 shows an improved performance during cooling as the T_{50} and T_{100} values are shifted to even lower temperatures. The catalytic performance of the initial CO oxidation experiment increases in the order Na-N-MnO_2 ≈ Na-OH-MnO_2 < K-OH-MnO_2 < K-N-MnO_2 < Moleculite ® < K-OH-MnO_2-450.

The results of the second CO oxidation experiment are not shown as the heating curve is identical to the cooling curve of the first CO oxidation experiment, and the cooling curve can be described by the heating curve of the third CO oxidation run.

The catalytic activities of Na-N-MnO_2 and Na-OH-MnO_2 during the third CO oxidation experiment are comparable to those of the first measurement, as the T_{50} temperatures are shifted to lower temperatures by less than 20 °C. Nevertheless, both samples achieve full conversion below 300 °C and exhibit no hysteresis between the heating and cooling curve of the third CO oxidation experiment. For K-N-MnO_2, the T_{50} temperature decreased by 23 °C compared with the initial CO oxidation, and full conversion was
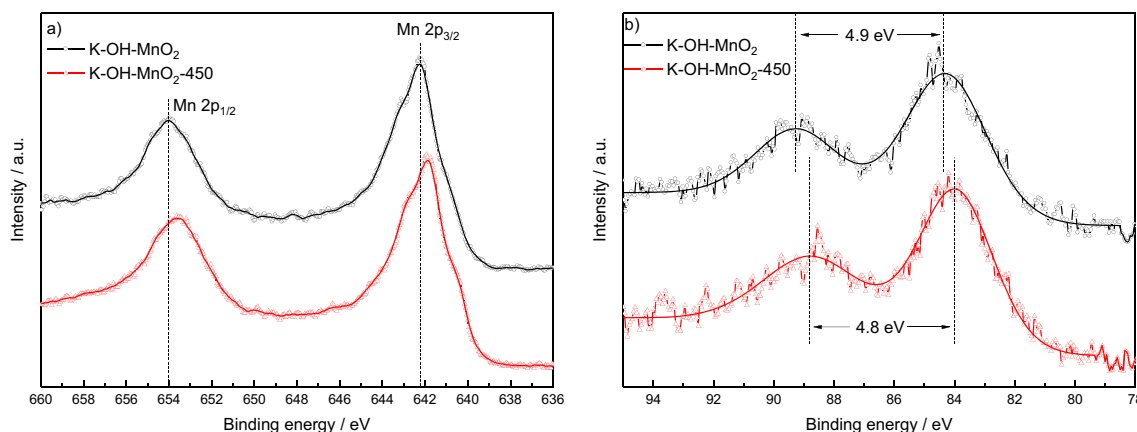
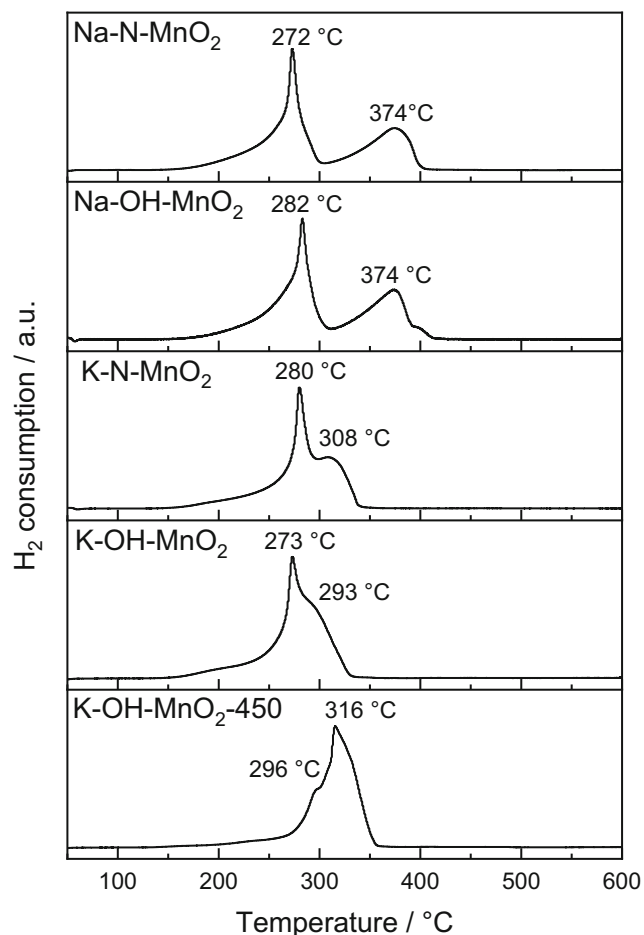**Fig. 5** Mn 2p (**a**) and Mn 3 s (**b**) spectra of K-OH-MnO_2 and K-OH-MnO_2-450

Fig. 6 H_2 TPR profiles of Na-N-MnO_2, Na-OH-MnO_2, K-N-MnO_2, K-OH-MnO_2, and K-OH-MnO_2-450

Fig. 7 CO TPR profiles of Na-N-MnO_2, Na-OH-MnO_2, K-OH-MnO_2, and K-OH-MnO_2-450

achieved at 255 °C. Only a negligible hysteresis can be observed between the heating and cooling curves of K-N-MnO_2. K-OH-MnO_2 displays the most interesting behavior, as a strong activation of the catalytic performance can be observed after CO oxidation at 450 °C. The T_{50} temperature during the heating decreased by 77 °C from the initial CO oxidation to the third CO oxidation experiment. After this activation, K-OH-MnO_2 has lower T_{50} and T_{100} temperatures than the commercial catalyst. The catalytic activity of K-OH-MnO_2-450 derived from the third CO oxidation is comparable to the
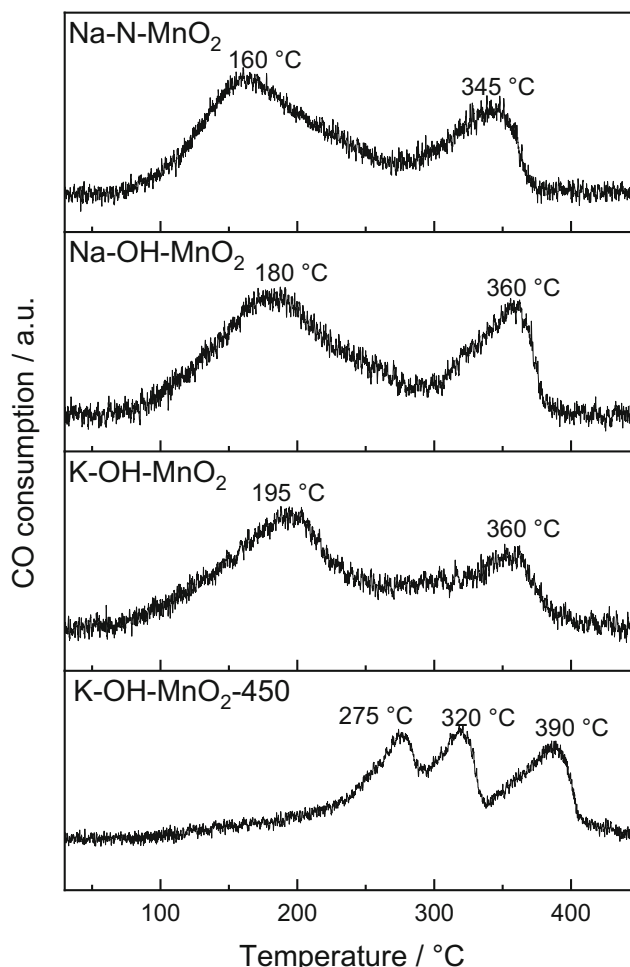
one of the first CO oxidation experiment as the T_{50} and T_{100} temperatures are shifted by less than 15 °C to higher temperatures. Nevertheless, K-OH-MnO_2-450 still has a higher catalytic activity than K-OH-MnO_2 and the commercial catalyst. Especially, the T_{100} temperature is significantly lower for K-OH-MnO_2-450 indicating a higher slope of the conversion curve. The catalytic performance after CO oxidation at 450 °C increases in the order Na-OH-MnO_2 < Na-N-MnO_2 < K-N-MnO_2 < Moleculite ® < K-OH-MnO_2 < K-OH-MnO_2-450. Both K-OH-MnO_2 and K-OH-MnO_2-450 are more

Table 5 Specific H_2 and CO consumption and degrees of reduction

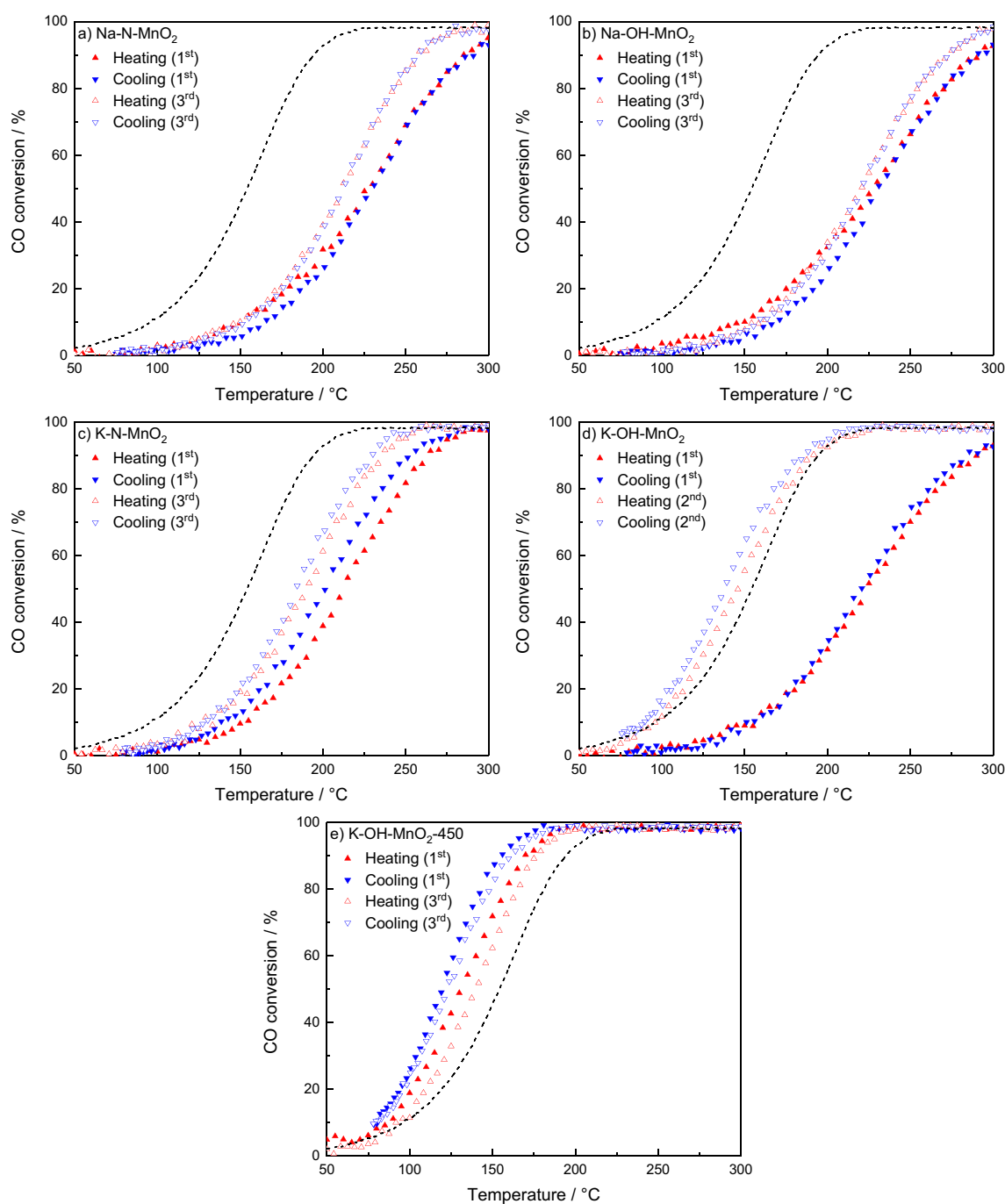| Sample	$n(H_2)$/mmol g^{-1}	$n(CO)$/mmol g^{-1}	Degree of reduction/%	
			H_2 TPR	CO TPR
Na-N-MnO_2	8.3	8.6	71.7	74.6
Na-OH-MnO_2	8.1	8.2	71.3	71.4
K-N-MnO_2	8.4	–	72.9	–
K-OH-MnO_2	7.9	8.0	68.6	69.3
K-OH-MnO_2-450	9.5	9.8	82.2	85.2

Fig. 8 CO conversion as a function of temperature during the first and third CO oxidation experiments for Na-N-MnO$_2$ (**a**), Na-OH-MnO$_2$ (**b**), K-N-MnO$_2$ (**c**), K-OH-MnO$_2$ (**d**), and K-OH-MnO$_2$-450 (**e**). CO conversion of Moleculite® is shown in each graph as a dashed line

catalytically active than the manganese copper-mixed oxide reference catalyst.

The assessment of the catalytic CO oxidation performance in comparison to catalysts reported in the literature is often difficult as various reaction conditions are applied. Tepluchin et al. [28] prepared MnO$_x$-based catalysts on γ-Al$_2$O$_3$ with metal loadings between 0.1 wt% and 20 wt%, which achieve almost full CO conversion at temperatures as low as 100 °C (20 wt%). However, it has to be noted that rather different

reaction conditions were used (500 mg of catalyst, 500 ppm CO, 5% O$_2$, total flow rate 250 mL min^{-1}). Catalysts based on precious metals such as Pt, Pd, or Rh have been extensively investigated for CO oxidation [29]. Typical Pt-based catalysts can reach full CO conversion at around 100 °C, but often reveal a huge hysteresis between the heating and the cooling ramp, because CO adsorption is so strong that no empty sites are left for O$_2$ activation at low temperatures [29, 30]. Such an inhibiting effect of CO is absent for MnO$_x$-based catalysts.

Table 6 T_{50} and T_{100} values during the heating and cooling ramps of the first CO oxidation run

Sample	Heating		Cooling	
	$T_{50}/$ °C	$T_{100}/$ °C	$T_{50}/$ °C	$T_{100}/$ °C
Moleculite®	155	220	145	215
Na-N-MnO$_2$	227	93%	231	93%
Na-OH-MnO$_2$	227	92%	232	92%
K-N-MnO$_2$	213	295	202	295
K-OH-MnO$_2$	222	93%	216	93%
K-OH-MnO$_2$-450	132	194	119	177

The XRD patterns of the four uncalcined samples after the CO oxidation experiments are shown in Fig. 9. An increased degree of crystallinity can be detected for all catalysts, but the XRD patterns after CO oxidation are rather different than the ones after calcination at 450 °C. The dominant phase of Na-N-MnO$_2$ after CO oxidation is α-Mn$_2$O$_3$ and only reflections with low intensity at 28.8° and 37.5° can be assigned to α-MnO$_2$. For Na-OH-MnO$_2$, reflections of α-Mn$_2$O$_3$ and α-MnO$_2$ were observed after CO oxidation. Due to the high intensity of the reflection at 32.9°, it can be assumed that α-Mn$_2$O$_3$ is the main phase of Na-OH-MnO$_2$. K-N-MnO$_2$ consists of a mixture of α-MnO$_2$ α-Mn$_2$O$_3$ after CO oxidation as indicated by reflections of similar intensity at 28.8°, 32.9°, and 37.5°. In contrast to the other three samples, the main phase of K-OH-MnO$_2$ can still be identified as α-MnO$_2$, but a small amount of α-Mn$_2$O$_3$ was formed as well.

Furthermore, the long-term stability of the catalytic performance was investigated for K-OH-MnO$_2$-450. Isothermal CO oxidation was performed at 150 °C for 125 h in a feed gas of 2% CO and 2% O$_2$ as shown in Fig. 10. CO conversion decreased from an initial value of 58% to a rather stable CO conversion of 42% after 125 h. A T_{50} temperature of 162 °C and a T_{100} temperature of 235 °C were derived from a subsequent CO

Table 7 T_{50} and T_{100} values during the heating and cooling ramps of the third CO oxidation run

Sample	Heating		Cooling	
	$T_{50}/$ °C	$T_{100}/$ °C	$T_{50}/$ °C	$T_{100}/$ °C
Moleculite®	160	255	160	255
Na-N-MnO$_2$	213	292	213	292
Na-OH-MnO$_2$	220	300	220	300
K-N-MnO$_2$	190	255	185	252
K-OH-MnO$_2$	145	231	138	225
K-OH-MnO$_2$-450	139	202	122	191

oxidation experiment up to 300 °C. After an additional O$_2$ pretreatment at 450 °C, the T_{50} and T_{100} temperatures decreased to 142 °C and 220 °C, respectively. Therefore, K-OH-MnO$_2$-450 still reveals a higher catalytic activity than the benchmark catalyst.

4 Discussion

The properties of the four uncalcined samples seem to be only weakly correlated with the type and amount of the incorporated alkali ion. The specific surface area, the crystallite size, and the particle morphology are almost identical for the uncalcined samples and do not change whether Na or K are used under either neutral or alkaline precipitation conditions. Therefore, it is proposed that these properties are predominantly determined by the spray-drying parameters controlling the quenching of crystallite growth. It is furthermore observed that alkaline precipitation conditions facilitate the incorporation of the alkali ions into the channel structure of MnO$_2$. A Mn 3s multiplet separation of $\Delta E = 4.9$ eV suggests that MnO$_2$ is the dominant surface oxidation state of the uncalcined samples although X-ray amorphous phases are obtained prior to calcination. The XRD results of the calcination series demonstrate that a certain amount of the alkali ions is necessary to stabilize the tunnel structure of α-MnO$_2$. K-N-MnO$_2$ and Na-N-MnO$_2$ precipitated under neutral conditions do not fully transform to α-MnO$_2$ after calcination at 450 °C. Due to the smaller amount of K/Na compared to alkaline samples, the α-MnO$_2$ tunnel structure is not stabilized and therefore, the phase transformation is not facilitated. After calcination at 500 °C K-N-MnO$_2$ and Na-N-MnO$_2$ form α-Mn$_2$O$_3$ as main phase further indicating insufficient stabilization. For K-OH-MnO$_2$ and Na-OH-MnO$_2$ precipitated under alkaline conditions, pure α-MnO$_2$ can be obtained after calcination at 450 °C. This is due to the higher amount of alkali ions stabilizing the tunnel structure. Furthermore, K has a stronger stabilizing effect than Na: K-OH-MnO$_2$ still forms pure α-MnO$_2$ after calcination at 500 °C, whereas a small amount of α-Mn$_2$O$_3$ is present in Na-OH-MnO$_2$-500.

The CO oxidation experiments show that the catalytic activity is strongly correlated with the phase composition of the samples. All uncalcined samples exhibit a similar catalytic performance during the first CO oxidation despite the different alkali ion content. Therefore, a direct promoting effect of the alkali ions on the catalytic activity of the Mn oxides was not observed. The reducibility of the uncalcined samples by H$_2$ is enhanced with increasing K content. However, as only the second reduction step from Mn$_3$O$_4$ to MnO is shifted to lower temperatures, this has no effect on the catalytic activity. Furthermore, the TPR experiments with CO suggest that the reducibility by CO is similar for all uncalcined samples and not enhanced by K indicating a different reduction mechanism
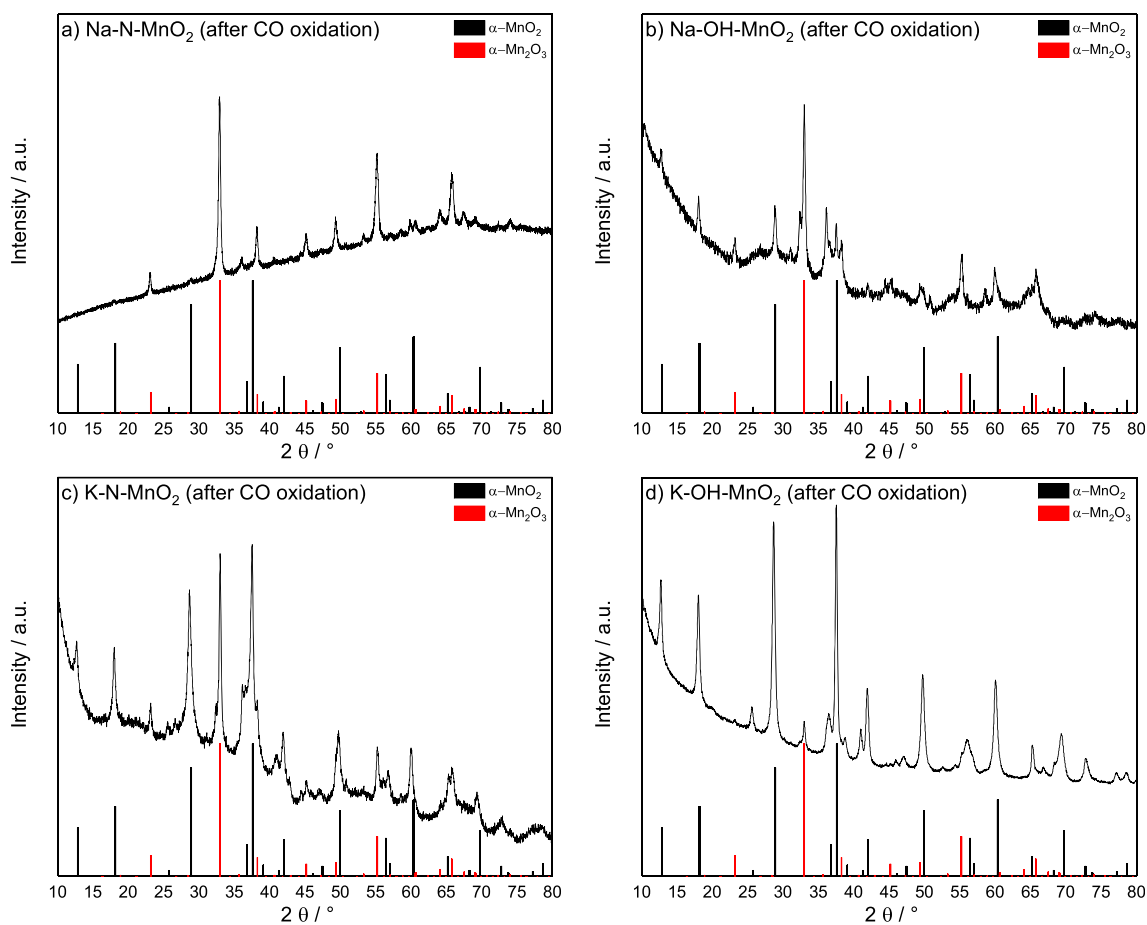
Fig. 9 XRD patterns of Na-N-MnO$_2$ (**a**), Na-OH-MnO$_2$ (**b**), K-N-MnO$_2$ (**c**), and K-OH-MnO$_2$ (**d**) after the CO oxidation experiments

by CO. An influence of the specific surface area, the crystallite size, or the particle morphology can be excluded as well, because these properties are almost identical. However, K-OH-MnO$_2$-450 containing pure α-MnO$_2$ shows a different three-step reduction process.
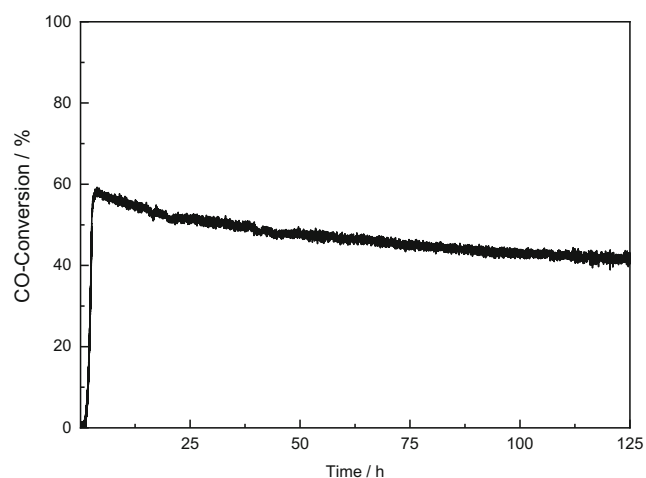

Fig. 10 CO conversion as a function of time over K-OH-MnO$_2$-450 at 150 °C

Even though the specific surface area of K-OH-MnO$_2$ decreased from 77 to 37 m^2 g^{-1} during calcination, the T_{50} and T_{100} values are shifted by almost 100 °C towards lower temperatures, indicating that the loss in specific surface area is compensated by favorable structural changes during the calcination treatment. The XRD results reveal that K-OH-MnO$_2$ is X-ray amorphous, whereas K-OH-MnO$_2$-450 is crystalline α-MnO$_2$. These observations are in good agreement with the results of Liang et al. [9], who showed that α-MnO$_2$ has the highest catalytic activity among the MnO$_2$ polymorphs. Furthermore, the higher degree of crystallinity of K-OH-MnO$_2$-450 may enhance the oxygen diffusion and oxygen mobility in the lattice [10]. Performing CO oxidation over K-OH-MnO$_2$ up to 450 °C drastically improves the catalytic performance during the cooling step as well as during the third CO oxidation experiment due to the formation of α-MnO$_2$. Because of the presence of traces of α-Mn$_2$O$_3$, the T_{50} and T_{100} values may be shifted to higher temperatures in comparison to K-OH-MnO$_2$-450. This strong activation upon heating is not observed for the other uncalcined samples, where primarily α-Mn$_2$O$_3$ with a high degree of crystallinity is formed after reaction at 450 °C. It is suggested that the increased degree of crystallinity after CO oxidation at 450 °C is

responsible for the slight increase in the catalytic activity of Na-N-MnO$_2$, Na-OH-MnO$_2$, and K-N-MnO$_2$. Nevertheless, the lower activities of the α-Mn$_2$O$_3$-containing samples demonstrate that the phase and oxidation state of Mn are the crucial factors for the catalytic activities. In addition to the favorable Mn–O bond strength, the high catalytic activity of α-MnO$_2$ can also be correlated to its different reduction behavior in comparison to the uncalcined samples. The CO TPR profiles suggest a three-step reduction process, which may enable a different CO oxidation pathway as well. The higher degree of reduction derived for K-OH-MnO$_2$-450 in comparison to the uncalcined samples indicates increased oxygen incorporation into the structure, which may also be beneficial for CO oxidation. Thus, these results indicate that the catalytic activity is not directly correlated with the reduction temperature of the samples, but rather with the reduction mechanism, as the less active uncalcined samples have lower reduction temperatures than K-OH-MnO$_2$-450.

Furthermore, the obtained phases after CO oxidation are in good agreement with the assumed stabilizing effect of Na$^+$ and K$^+$ on the tunnel structure of α-MnO$_2$. It can be assumed that under the stronger reducing reaction conditions, α-Mn$_2$O$_3$ is formed more readily than during calcination at 450 °C. Therefore, α-Mn$_2$O$_3$ is formed predominantly for Na-N-MnO$_2$, Na-OH-MnO$_2$, and K-N-MnO$_2$ as Na has a weaker stabilizing effect than K and K-N-MnO$_2$ has a lower K content than K-OH-MnO$_2$. Nevertheless, bulk Mn$_3$O$_4$ or MnO cannot be identified after the reaction, even though the complete reduction is achieved below 450 °C for the samples during TPR with either H$_2$ or CO, indicating that MnO is readily reoxidized to α-MnO$_2$ or α-Mn$_2$O$_3$ under reaction conditions. Thus, it can be concluded that the promoting effect of K on the catalytic activity of Mn oxides is predominantly caused by its stabilizing effect on the structure of α-MnO$_2$ keeping the samples in their catalytically most active state.

Further studies are in progress addressing the long-term stability of the synthesized samples and especially of the α-MnO$_2$ structure at higher reaction temperatures. Moreover, the influence of H$_2$O on the catalytic performance has to be examined, because it is a critical component of industrial exhaust gases with a strong impact on solid-state transformations.

5 Conclusions

MnO$_2$ catalysts with incorporated Na$^+$ or K$^+$ ions were successfully synthesized by a semi-continuous precipitation method based on spray drying. The as-received samples were shown to be X-ray amorphous, whereas pure α-MnO$_2$ was obtained after calcination at 450 °C of a K-containing catalyst precipitated in 0.01 M KOH solution. All catalysts were found to be active in catalytic CO oxidation and reached full conversion below 300 °C. The catalytic activity of the samples is mainly correlated to the phase composition and Mn oxidation state rather than to the type or amount of the alkali metal. Crystalline α-MnO$_2$ exhibits an exceptional catalytic activity and performs better than a commercial manganese copper-mixed oxide catalyst, whereas X-ray amorphous MnO$_2$ as well as Mn$_2$O$_3$ have higher T_{50} and T_{100} temperatures than α-MnO$_2$. Furthermore, it was possible to achieve a significant enhancement of the catalytic activity of an uncalcined K-containing catalyst under reaction conditions at 450 °C, which is caused by the formation of crystalline α-MnO$_2$. The beneficial effect on the catalytic activity observed for K incorporation can be mainly attributed to the stabilization of the α-MnO$_2$ tunnel structure during thermal treatment. When the catalysts contain Na or an insufficient amount of K, less active phases such as Mn$_2$O$_3$ are formed.

References

1. Bürgi, T., Bieri, M.: Time-resolved in situ ATR spectroscopy of 2-propanol oxidation over Pd/Al$_2$O$_3$. Evidence for 2-propoxide intermediate. J. Phys. Chem. B. **108**(35), 13364–13369 (2004). https://doi.org/10.1021/jp048187u
2. Su, E.C., Montreuil, C.N., Rothschild, W.G.: Oxygen storage capacity of monolith three-way catalysts. Appl. Catal. **17**(1), 75–86 (1985). https://doi.org/10.1016/S0166-9834(00)82704-9
3. Liu, K., Wang, A., Zhang, T.: Recent advances in preferential oxidation of CO reaction over platinum group metal catalysts. ACS Catal. **2**(6), 1165–1178 (2012). https://doi.org/10.1021/cs200418w
4. Wang, J., Chen, H., Hu, Z., Yao, M., Li, Y.: A review on the Pd-based three-way catalyst. Catal. Rev. **57**(1), 79–144 (2014). https://doi.org/10.1080/01614940.2014.977059
5. Nibbelke, R.H., Nievergeld, A.J.L., Hoebink, J.H.B.J., Marin, G.B.: Development of a transient kinetic model for the CO oxidation by O2 over a Pt/Rh/CeO$_2$/γ-Al$_2$O$_3$ three-way catalyst. Appl. Catal. B Environ. **19**(3-4), 245–259 (1998). https://doi.org/10.1016/S0926-3373(98)00076-9
6. Chatterjee, D., Deutschmann, O., Warnatz, J.: Detailed surface reaction mechanism in a three-way catalyst. Faraday Disc. **119**(1), 371–384 (2001). https://doi.org/10.1039/B101968F
7. Hedjazi, K., Zhang, R., Cui, R., Liu, N., Chen, B.: Synthesis of TiO$_2$ with diverse morphologies as supports of manganese catalysts for CO oxidation. Appl. Petrochem. Res. **6**(1), 89–96 (2016). https://doi.org/10.1007/s13203-015-0141-y
8. Ramesh, K., Chen, L., Chen, F., Liu, Y., Wang, Z., Han, Y.-F.: Re-investigating the CO oxidation mechanism over unsupported MnO, Mn$_2$O$_3$ and MnO$_2$ catalysts. Catal. Today. **131**(1-4), 477–482 (2008). https://doi.org/10.1016/j.cattod.2007.10.061
9. Liang, S., Teng, F., Bulgan, G., Zong, R., Zhu, Y.: Effect of phase structure of MnO$_2$ nanorod catalyst on the activity for CO oxidation. J. Phys. Chem. C. **112**(14), 5307–5315 (2008). https://doi.org/10.1021/jp0774995
10. Wagloehner, S., Nitzer-Noski, M., Kureti, S.: Oxidation of soot on manganese oxide catalysts. Chem. Eng. J. **259**, 492–504 (2015). https://doi.org/10.1016/j.cej.2014.08.021

11. Sihaib, Z., Puleo, F., Garcia-Vargas, J.M., Retailleau, L., Descorme, C., Liotta, L.F., Valverde, J.L., Gil, S., Giroir-Fendler, A.: Manganese oxide-based catalysts for toluene oxidation. Appl. Catal. B Environ. **209**, 689–700 (2017). https://doi.org/10.1016/j.apcatb.2017.03.042

12. Stobbe, E.R., de Boer, B.A., Geus, J.W.: The reduction and oxidation behaviour of manganese oxides. Catal. Today. **47**(1-4), 161–167 (1999). https://doi.org/10.1016/S0920-5861(98)00296-X

13. Liu, Y., Wang, H., Zhu, Y., Wang, X., Liu, X., Li, H., Qian, Y.: Pyrolysis synthesis of magnetic - and -MnO$_2$ nanostructures and the polymorph discrimination. Solid State Commun. **149**(37-38), 1514–1518 (2009). https://doi.org/10.1016/j.ssc.2009.06.008

14. Liu, Y., Wei, J., Tian, Y., Yan, S.: The structure–property relationship of manganese oxides. Highly efficient removal of methyl orange from aqueous solution. J. Mater. Chem. A. **3**(37), 19000–19010 (2015). https://doi.org/10.1039/C5TA05507E

15. Yin, B., Zhang, S., Jiang, H., Qu, F., Wu, X.: Phase-controlled synthesis of polymorphic MnO$_2$ structures for electrochemical energy storage. J. Mater. Chem. A. **3**(10), 5722–5729 (2015). https://doi.org/10.1039/C4TA06943A

16. Feng, Q., Yanagisawa, K., Yamasaki, N.: Hydrothermal soft chemical process for synthesis of manganese oxides with tunnel structures. J. Porous. Mater. **5**(2), 153–162 (1998). https://doi.org/10.1023/A:1009657724306

17. Muraoka, Y., Chiba, H., Atou, T., Kikuchi, M., Hiraga, K., Syono, Y., Sugiyama, S., Yamamoto, S., Grenier, J.-C.: Preparation of α-MnO$_2$ with an open tunnel. J. Solid State Chem. **144**(1), 136–142 (1999). https://doi.org/10.1006/jssc.1999.8133

18. Frey, K., Iablokov, V., Sáfrán, G., Osán, J., Sajó, I., Szukiewicz, R., Chenakin, S., Kruse, N.: Nanostructured MnO$_x$ as highly active catalyst for CO oxidation. J. Catal. **287**, 30–36 (2012). https://doi.org/10.1016/j.jcat.2011.11.014

19. Iablokov, V., Frey, K., Geszti, O., Kruse, N.: High catalytic activity in CO oxidation over MnO$_x$ nanocrystals. Catal. Lett. **134**(3-4), 210–216 (2010). https://doi.org/10.1007/s10562-009-0244-0

20. Qian, K., Qian, Z., Hua, Q., Jiang, Z., Huang, W.: Structure–activity relationship of CuO/MnO$_2$ catalysts in CO oxidation. Appl. Surf. Sci. **273**, 357–363 (2013). https://doi.org/10.1016/j.apsusc.2013.02.043

21. Chang, Y.-f., McCarty, J.G.: Novel oxygen storage components for advanced catalysts for emission control in natural gas fueled vehicles. Catal. Today. **30**(1-3), 163–170 (1996). https://doi.org/10.1016/0920-5861(95)00007-0

22. Sing, K.S.W., Williams, R.T.: Physisorption hysteresis loops and the characterization of nanoporous materials. Adsorpt. Sci. Technol. **22**(10), 773–782 (2016). https://doi.org/10.1260/0263617053499032

23. Burgess, C.G.V., Everett, D.H.: The lower closure point in adsorption hysteresis of the capillary condensation type. J. Colloid Interface Sci. **33**(4), 611–614 (1970). https://doi.org/10.1016/0021-9797(70)90014-7

24. Jiang, J., Kucernak, A.: Electrochemical supercapacitor material based on manganese oxide. Preparation and characterization. Electrochim. Acta. **47**(15), 2381–2386 (2002). https://doi.org/10.1016/S0013-4686(02)00031-2

25. Biesinger, M.C., Payne, B.P., Grosvenor, A.P., Lau, L.W.M., Gerson, A.R., Smart, R.S.C.: Resolving surface chemical states in XPS analysis of first row transition metals, oxides and hydroxides. Cr, Mn, Fe, Co and Ni. Appl. Surf. Sci. **257**(7), 2717–2730 (2011). https://doi.org/10.1016/j.apsusc.2010.10.051

26. Ilton, E.S., Post, J.E., Heaney, P.J., Ling, F.T., Kerisit, S.N.: XPS determination of Mn oxidation states in Mn (hydr)oxides. Appl. Surf. Sci. **366**, 475–485 (2016). https://doi.org/10.1016/j.apsusc.2015.12.159

27. Wu, Y., Liu, M., Ma, Z., Xing, S.T.: Effect of alkali metal promoters on natural manganese ore catalysts for the complete catalytic oxidation of o-xylene. Catal. Today. **175**(1), 196–201 (2011). https://doi.org/10.1016/j.cattod.2011.04.023

28. Tepluchin, M., Casapu, M., Boubnov, A., Lichtenberg, H., Wang, D., Kureti, S., Grunwaldt, J.-D.: Fe and Mn-based catalysts supported on γ-Al$_2$O$_3$ for CO oxidation under O$_2$-rich conditions. ChemCatChem. **6**(6), 1763–1773 (2014). https://doi.org/10.1002/cctc.201301040

29. Zhou, Y., Wang, Z., Liu, C.: Perspective on CO oxidation over Pd-based catalysts. Catal. Sci. Technol. **5**(1), 69–81 (2014). https://doi.org/10.1039/C4CY00983E

30. Al Soubaihi, R., Saoud, K., Dutta, J.: Critical review of low-temperature CO oxidation and hysteresis phenomenon on heterogeneous catalysts. Catalysts. (2018). https://doi.org/10.3390/catal8120660

Publisher's Note Springer Nature remains neutral with regard to jurisdictional claims in published maps and institutional affiliations.